Computers and Chemical Engineering 78 (2015) 24–38

Contents lists available at ScienceDirect

Computers and Chemical Engineering

journal homepage: www.elsevier.com/locate/compchemeng

# Fully coupled LES-DEM of particle interaction and agglomeration in a turbulent channel flow

M. Afkhami, A. Hassanpour*, M. Fairweather, D.O. Njobuenwu

*Institute of Particle Science and Engineering, School of Chemical and Process Engineering, University of Leeds, Leeds LS2 9JT, UK*

ARTICLE INFO

*Article history:*
Received 9 July 2014
Received in revised form 4 February 2015
Accepted 5 April 2015
Available online 11 April 2015

*Keywords:*
Large eddy simulation
Discrete element method
Two-phase flow
Agglomeration
Channel

ABSTRACT

Coupled large eddy simulation and the discrete element method are applied to study turbulent particle–laden flows, including particle dispersion and agglomeration, in a channel. The particle–particle interaction model is based on the Hertz–Mindlin approach with Johnson–Kendall–Roberts cohesion to allow the simulation of van der Waals forces in a dry air flow. The influence of different particle surface energies, and the impact of fluid turbulence, on agglomeration behaviour are investigated. The agglomeration rate is found to be strongly influenced by the particle surface energy, with a positive relationship observed between the two. Particle agglomeration is found to be enhanced in two separate regions within the channel. First, in the near-wall region due to the high particle concentration there driven by turbophoresis, and secondly in the buffer region where the high turbulence intensity enhances particle–particle interactions.



## 1. Introduction

Understanding the fundamental aspects of turbulent fluid–particle flows is of relevance to processes employed in a wide range of applications, such as oil and gas flow assurance in pipes, powder dispersion from dry powder inhalers and particle re-suspension in nuclear waste ponds. Despite their importance, little is known about the influence of inter-particle collisions on the particle and fluid phase characteristics in the context of particle dispersion, agglomeration and deposition in such turbulent, bounded flows laden with large particle numbers.

Particle–laden flows can be classified into three general categories with respect to their inter-particle collisions: dilute (collision-free) flows, medium concentration (collision-dominated) flows, and dense (contact-dominated) flows (Tsuji, 2000). For a poly-dispersed particle flow, these inter-particle collisions can be easily related to the particle volume fraction, $\varphi_p = \sum_N V_p/V$ which simplifies to $\varphi_p = NV_p/V$ for a mono-dispersed particle size, where $N$ is the number of particles, $V_p$ the volume of a particle, and $V$ the volume that the particles and fluids occupy (Elghobashi, 1991). It is acknowledged that most practical systems are poly-dispersed; however, it is necessary to understand the physics of a simple system before moving to a more complex one.

In two-phase flows, the physical parameters that are the most influential on flow and particle behaviour are the particle Stokes number, which quantifies the response of the dispersed phase to the perturbations created by the turbulence field, and the flow Reynolds number. Other important parameters are those associated with fluid–particle interaction (one-way/two-way coupling), particle–particle interaction (collision models), particle–wall interaction (reflecting or absorbing wall, and wall effects), particle rotation and the various forces acting on the particles (e.g. the hydrodynamic forces). Conventionally, the flow is considered to be a dilute suspension and one-way coupled for a particle volume fraction less than $10^{-6}$, with the trajectory of the particles controlled by the carrier phase and with the particles having a negligible effect on the flow. For a particle volume fraction in the range $10^{-6}$–$10^{-3}$, the flow is considered to be a dilute suspension and two-way coupled, with the particles having an effect on the carrier flow. Such flows are encountered in dilute conveying, where oscillations and excursions in gas pressure are lowered due to the distributed nature of the particles in the fluid, thereby providing a stable method of particle transport (Lim et al., 2006a). Finally, if the volume fraction is greater than $10^{-3}$, the flow is considered to be four-way coupled, with the particles having an effect on the carrier fluid and with particle motion significantly influenced by particle–particle interactions. Such flows are observed in dense conveying, where the shear and collisional forces are usually low, with this method of

* Corresponding author. Tel: +44 113 3432405
*E-mail address:* a.hassanpour@leeds.ac.uk (A. Hassanpour).

http://dx.doi.org/10.1016/j.compchemeng.2015.04.003

transport therefore favoured in the conveyance of solids sensitive to abrasion.

This work focuses on dilute and medium concentration flows; generally, a dilute flow can be described as one in which the motion of the particles is considered to be unaffected by the surrounding particles and is only controlled by the surface and body forces acting on them (Crowe et al., 1996). This is only valid, however, for particles of low Stokes number. At higher Stokes numbers, particle–particle interactions are common in both horizontal and vertical wall-bounded dilute turbulent flows due to the effects of gravity and fluid turbulence, respectively.

Recent literature involving a one-way coupled approach has concerned prediction of the behaviour of particles in complex turbulent flows, with the aim of providing physical insight into particle dispersion characteristics in such flows. A number of direct numerical simulation (DNS) and large eddy simulation (LES) studies of continuous flows through channels have been carried out (e.g. Marchioli et al. 2008). Other notable one-way coupled studies include those of Eskin (2005) and Winkler et al. (2006) who considered, amongst other things, the influence of wall roughness in a turbulent channel flow, and particle deposition in a turbulent square duct flow, with the latter authors also examining the influence of two- and four-way coupling on particle deposition. Fairweather and Yao (2009) used LES coupled to a Lagrangian particle tracking (LPT) algorithm to analyse particle dispersion mechanisms in a turbulent square duct flow, with Vinkovic et al. (2011) adopting a DNS-LPT approach to study the characteristics of solid particles that interact with fluid ejections in dilute turbulent channel flow. Jaszczur (2011) also used LES to study particle–fluid interaction in a channel flow, comparing results with predictions based on DNS, whilst Gao et al. (2012) employed a Reynolds-averaged Navier–Stokes approach, coupled to a Lagrangian particle tracker, to predict particle deposition in a vertical channel flow. Njobuenwu and Fairweather (2014) also used an LES-based approach to study the effect of shape on inertial particle dynamics in a channel flow.

Flows are considered to be two-way coupled when there is a mutual interaction between the particles and the fluid; the turbulent flow influences the particle trajectory and the particle itself influences the flow. Two-way coupling arises when the fluid contains a sufficient number of particles, and in such cases a loss or gain in the momentum of the turbulent flow is caused by them (Squires and Eaton, 1990). Particles impact on the carrier flow in a number of ways, including the wake generation of turbulence, streamline distortion, alteration of velocity gradients, and turbulence generation or damping owing to the drag forces on the particles (Crowe, 2000). When examining the effect of particles on a flow a number of factors are important, including the particle size and shape, the relative density between the fluid and the particle, and the motion of the particles (Humphrey et al., 1990). A number of recent studies on two-way coupled channel flow include those of Zhao et al. (2010) who considered turbulence modulation and drag reduction by spherical particles, Zhao (2011) who used DNS to investigate the impact of non-spherical particles, and Zhao et al. (2012) who considered Stokes number effects on the particle slip velocity in wall-bounded turbulence and their implication for dispersion models. Andersson et al. (2012) also studied torque-coupling and particle–turbulence interactions, with a number of other works by the same authors considering the modelling of particle stress, particle spin, and particle suspensions in two-way coupled gas–solid turbulent channel flows.

The particle–particle interactions occurring in four-way coupled flows are usually only considered in dense flows, which exhibit very complex behaviour and have only relatively recently been studied using computational modelling techniques. When considering dense flows it is important that inter-particle collisions are taken into account (Elghobashi, 1991).

Sundaram and Collins (1999) investigated turbulence modification by particles, together with the effect of inter-particle collisions, in isotropic turbulence using DNS. Yamamoto et al. (2001) studied similar flows, with the gas phase and particle trajectories predicted using large eddy simulation and a Lagrangian approach that included inter-particle collisions based on a deterministic method. When considering such collisions, it was found that the shape and scale of particle concentrations calculated were in agreement with experimental data. It was also established that inter-particle collisions resulted in transverse mixing which led to the flattening of particle velocity and concentration profiles. Nasr and Ahmadi (2007) examined the effect of two-way coupling and inter particle collisions on turbulence modification in a vertical channel flow. The dispersed phase was simulated using a Lagrangian particle tracking approach that considered gravity, the Saffman lift force, particle collisions and particle–wall interactions. Predictions were compared against those of Kulick et al. (1994) and Yamamoto et al. (2001), with the results demonstrating that the inclusion of particle–particle interactions gave rise to attenuation in the turbulence intensity compared to an augmentation when the particle–particle collisions were ignored.

In the four-way coupled methodology, the bidirectional interaction of particles with the flow and between particles is considered, with this method frequently utilised to simulate pneumatic conveying systems. In a horizontal bounded flow, for example, a wave-like plug flow can be formed which sweeps up any stationary particles that deposit within the flow. The particle velocity is almost invariable throughout the plug, although the relative slip velocity of particles in the near-wall region is large. These characteristics have been studied using computational fluid dynamic (CFD) approaches coupled to the discrete element (DEM) method by a number of authors (Tsuji et al., 1992; Xiang and McGlinchey, 2004; Li and Kuipers, 2005; Li and Mason, 2000; Lim et al., 2006a,b; Fraige and Langston, 2006; Zhang and Thornton, 2007; Kuang et al., 2008; Chu and Yu, 2008). Li et al. (2005) investigated the influence of the stationary layer in the lower half of a pipe on the transition and flow of slugs, with details of the flow mechanism considered. The authors demonstrated the formation, breakdown and motion of one plug, and the stationary layer left behind. The particles were seen to shift from the slug to the stationary layer as the plug moved along the pipe, with significant changes in the solids' concentration, pressure and velocity distributions across the slug. As the slug wave progressed it compressed the particle layer and forced some of the particles upwards from the layer into the wave. The particles towards the rear of the slug also dropped into the lower section of the pipe and created a stationary particle layer behind the slug. All these characteristics were verified against video recordings. Fraige and Langston (2006) further investigated the flow in a horizontal pipe, considering the influence of material properties on the flow characteristics. Kuang et al. (2008) studied the microscopic and macroscopic structures of slug flow, noting that the slug velocity increases linearly in relation to the gas flow rate and is unaffected by the solid flow rate, with the slug length increasing with both. In vertical pneumatic conveying, CFD-DEM studies have shown that for systems of low particle concentration and high gas velocity, the particles are inclined to be dispersed throughout the pipe cross-section, whilst for high solid concentrations and low gas velocities, the particles form clusters and move as a dense plug (Kawaguchi, 2000; Ouyang et al., 2005; Lim et al., 2006a; Xu et al., 2007; Zhang et al., 2008; Chu and Yu, 2008), with these results in line with experimental observations (Zhu and Yu, 2003). For further information on the development of CFD-DEM the reader is referred to the review papers by Deen et al. (2007) and Zhu et al. (2008). More recent work on four-way

coupled flows includes that of Vreman et al. (2009) who used a two- and four-way coupled Eulerian–Lagrangian approach based on LES, and Pirker et al. (2010) who employed the discrete element method coupled with fluid flow calculations and an Eulerian granular model to study horizontal conveying through a duct with a square cross-section. The emphasis in the latter work was related to the break-up of particle 'ropes' that consisted of very coarse particles produced by a spiral inlet to the duct. Calvert et al. (2011, 2013) used DEM coupled to a continuum model to investigate the aerodynamic dispersion of cohesive clusters with different particle surface energies and size, respectively. The authors found a strong relationship between cluster dispersion and particle surface energy and cluster size. Pan et al. (2011) used a unified second-order moment stress model with the kinetic theory of granular flows in an Eulerian–Eulerian, two-fluid approach to investigate gas–particle flows in a horizontal channel under reduced gravity environments, with Alvandifar et al. (2011) basing their model on a source-term formulation and a deterministic approach for the particles, and coupling terms representing the fluid-particle interactions. Chen et al. (2011) used DNS with a hard sphere model for particles, with Laín and Sommerfeld (2011) employing an Eulerian–Lagrangian approach within a Reynolds-averaged Navier–Stokes modelling framework. Mohaupt et al. (2011) used a new approach based on the stochastic paths of particles, with Wang et al. (2011) studying particle deposition on a wall driven by turbulence, thermophoresis and particle agglomeration in a vertical channel flow. Lastly, Laín and Sommerfeld (2012) focused on the effect of wall roughness on the particle concentration distribution across a channel and the velocity characteristics of both the fluid and particle phases by accounting for full coupling between the phases.

Based on the most recent work on two-phase channel flows, it is clear that the DNS studies performed are for low Reynolds number flows, and hence LES is required if high Reynolds numbers flows of practical relevance are to be accurately predicted. Furthermore, the complications that arise when analysing the underlying mechanisms that dictate particle dispersion in such flows require the level of detail that is provided by a CFD-DEM approach, as shown by the noteworthy successes of the technique noted above. In this work, therefore, LES is coupled with the discrete element method to provide further understanding of particle–laden flows, in particular in relation to how particles interact in a turbulent channel flow, and how those interactions result in the formation of agglomerates which affect the dispersion and deposition of the particles within the flow.

## 2. Numerical simulation approach

In this work the fluid phase is calculated using an Eulerian large eddy simulation which is capable of accurately predicting complex dynamic flow phenomena. In the coupled Eulerian–Lagrangian approach a large number of individual point particles are simultaneously tracked for the dispersed phase. The bidirectional interaction of the particles with the flow and between the particles is considered, thus creating a four-way coupled methodology for simulating turbulent particle–laden flow. In the following the basic features of the methods used are described. For further information the reader is referred to the citations given.

### 2.1. Large eddy simulation

#### 2.1.1. Governing equations

In LES, only the largest and most energetic scales of motions are directly computed, whilst the small scales are modelled (Smagorinsky, 1963). Any function is decomposed using a localised filter function such that filtered values only retain the variability of the original function over length scales comparable with or larger than that of the filter width. This decomposition is then applied to the Navier–Stokes equations, for an incompressible Newtonian fluid with constant properties, bringing about terms which represent the effect of the sub-grid scale (SGS) motion on the resolved motion. The governing equations are:

$$\frac{\partial \bar{u}_i}{\partial t} + \frac{\partial \bar{u}_i \bar{u}_j}{\partial x_j} = -\frac{1}{\rho}\frac{\partial \bar{p}}{\partial x_i} - \frac{\partial \tau_{ij}}{\partial x_j} + \frac{\partial}{\partial x_j}\left(\nu \frac{\partial \bar{u}_i}{\partial x_j}\right) + f_i \tag{1}$$

$$\frac{\partial \bar{u}_i}{\partial x_i} = 0 \tag{2}$$

where $u_i$, $p$ and $\nu$ are the velocity components, the pressure and the kinematic viscosity, respectively. The term $f_i$ denotes a source term (momentum sink) resulting from the particulate phase (Alletto and Breuer, 2012), and the overbar ($-$) denotes the resolved scales. The filtering of the non-linear convective term in the momentum (1), gives rise to the additional SGS stress tensor $\tau_{ij}$ which has to mimic the influence of the non-resolved small-scale turbulence on the resolved large scale turbulent eddies. The sub-grid scale stress, $\tau_{ij}$ is defined by;

$$\tau_{ij} = \bar{u_i u_j} - \bar{u}_i \bar{u}_j \tag{3}$$

This stress, which results from the filtering operation in (3), is unknown and needs closure. In this work, a model based on the eddy-viscosity concept was used to compute the SGS from:

$$\tau_{ij}^a = \tau_{ij} - \frac{1}{3}\tau_{kk}\delta_{ij} = -2\nu_t \bar{S}_{ij} \tag{4}$$

where $\tau_{ij}^a$ is the anisotropic (traceless) part of the stress tensor $\tau_{ij}$, $\nu_t$ is the SGS eddy-viscosity, $\delta_{ij}$ is the Kronecker delta, and $\bar{S}_{ij}$ is the resolved rate-of-strain tensor defined as $\bar{S}_{ij} = 1/2\left(\partial \bar{u}_i/\partial x_j + \partial \bar{u}_j/\partial x_i\right)$. It is now required to determine the SGS viscosity, $\nu_t$. The trace of the stress tensor is added to the pressure forming a new pressure $P = \bar{p} + \tau_{kk}/3$. The eddy viscosity $\nu_t$ itself is a function of the strain rate tensor $\bar{S}_{ij}$ and the sub-grid length $l$, according to:

$$\nu_t = C_\nu \bar{\Delta}^2 |\bar{S}| \text{ with } |\bar{S}| = \sqrt{2\bar{S}_{ij}\bar{S}_{ij}} \tag{5}$$

where $C_\nu$ is a model constant, $|\bar{S}|$ is the modulus of the rate-of-strain for the resolved scales, and $\bar{\Delta}$ is the grid-filter width given by $\bar{\Delta} = V^{1/3}$. The sub-grid scale stress is therefore,

$$\tau_{ij} - \frac{\delta_{ij}}{3}\tau_{kk} = -2C_\nu \bar{\Delta}^2 |\bar{S}| \bar{S}_{ij} \tag{6}$$

This simple model is both economic and robust, however, the practical shortcoming is that it is limited to a single value of the model constant ($C_\nu$) which is not universally applicable to a wide range of flows. Germano et al. (1991) and subsequently Lilly (1992) proposed a dynamic procedure which has been used in this work. The choice of dynamic sub-grid scale model was based on sensitivity studies carried out using different models and also sensitivity studies in the literature for the same code, for example Abdilghanie et al. (2009). In this model the Smagorinsky constant, $C_\nu$, is computed as a function of time and space based on the information provided by the resolved scales of motion. This requires a test filter ($\tilde{\Delta}$) to acquire the small scales of the resolved field. It is common to denote the test-filtered quantities by a tilde, and write the filtered Navier–Stokes equations as the test-filtered Navier–Stokes equations (Kim, 2004). The stress associated with the smallest resolved scales between the test-filter scale ($\tilde{\Delta}$) and the grid-filter scale ($\bar{\Delta}$) can be interpreted as the stress components, $L_{ij}$, which can be

directly obtained from the resolved scales and used to calculate the model constant.

$$L_{ij} - \frac{\delta_{ij}}{3}L_{kk} = C_v(\alpha_{ij} - \tilde{\beta}_{ij}) \tag{7}$$

$$\text{where} \quad \alpha_{ij} = -2\tilde{\Delta}^2|\tilde{\bar{S}}|\tilde{\bar{S}}_{ij} \quad \text{and} \quad \beta_{ij} = -2\bar{\Delta}^2|\tilde{\bar{S}}|\tilde{\bar{S}}_{ij} \tag{8}$$

Based on Lilly's suggestion, the model constant $C_v$ is calculated by determining the value of $C_v$ which reduces the square of the errors given by:

$$E = \left(L_{ij} - \frac{\delta_{ij}}{3}L_{kk} - C_v M_{ij}\right)^2 \tag{9}$$

where

$$M_{ij} = \alpha_{ij} - \tilde{\beta}_{ij} = -2(\tilde{\Delta}^2|\tilde{\bar{S}}|\tilde{\bar{S}}_{ij} - \bar{\Delta}^2|\tilde{\bar{S}}|\tilde{\bar{S}}_{ij}) \tag{10}$$

Taking $\partial E/\partial C_v$ and setting it zero gives:

$$C_v = \frac{L_{ij}M_{ij}}{M_{ij}M_{ij}} \tag{11}$$

As a result, the model constant $C_v$ calculated is a local value that varies in time and space, taking both negative and positive values. A negative $C_v$ gives rise to a negative eddy-viscosity which is caused by the flow of energy from the sub-grid scale eddies to the resolved eddies (i.e. "back-scatter") and considered an advantageous aspect of dynamic models. A very large negative eddy viscosity can, however, bring about numerical instability, giving rise to a high level of numerical noise or even divergence of the numerical solution. To prevent this, $C_v$ is cut-off at zero. This is somewhat different to the conventional approach in which the total viscosity (laminar viscosity plus eddy-viscosity) is limited, therefore permitting a small negative SGS eddy-viscosity.

The dynamic approach requires a test filter. One deciding factor in selecting the test-filter is that it should be consistent with the grid-filter. To meet this condition, this work employed a top-hat filter as it fits naturally into a finite-volume formulation. Moreover, the test-filter ought to be applicable to unstructured meshes:

$$\tilde{\bar{\phi}}(c_0) = \frac{1}{\Sigma_n V_i}\int_{V_{tot}} \bar{\phi}dv = \frac{\Sigma_i \bar{\phi}_i V_i}{\Sigma_i V_i} \tag{12}$$

### 2.1.2. Numerical solution method

The code implements an implicit finite-volume incompressible flow solver using a co-located variable storage arrangement. Because of this arrangement, a procedure similar to that outlined by Rhie and Chow (1983) is used to prevent checkerboarding of the pressure field. In the segregated solver, diffusion terms are discretised using a central differencing scheme. The governing equations are solved in a sequential (segregated) manner. The discretised algebraic equations are solved using a point-wise Gauss–Seidel iterative algorithm. An algebraic multi-grid method is employed to accelerate solution convergence. For temporal discretisation, the segregated solver uses a three-level, second-order scheme. Time advancement is performed via an implicit method for all transport terms (based on a generalised fractional-step procedure), with the overall procedure second-order accurate in both space and time. The splitting error can be driven to zero if the sub-iterations are carried out per time-step. Initially, an adaptive time-step was chosen, based on the estimation of a truncation error of 0.01 associated with the time integration scheme. If the truncation error was smaller than a specified tolerance, the size of the time-step was increased, and vice versa. This process continued until a constant time-step value was reached which was subsequently implemented as a fixed value. The code is parallel and uses the message passing interface HP-MPI. Time-averaged flow field variables were computed from running averages during the computations. Further information on the mathematical model employed, and the numerical solution algorithm and its application, may be found in the ANSYS Fluent 13.0 theory guide.

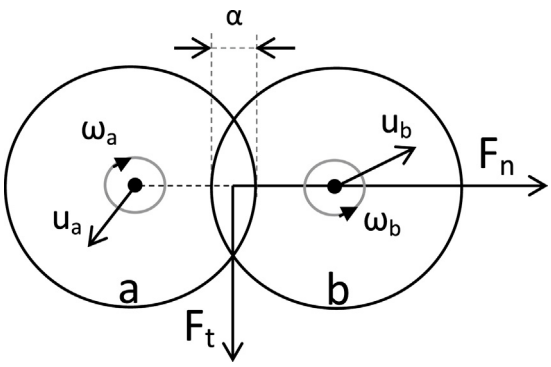


**Fig. 1.** Schematic representation of the discrete particle collision model (after Deen et al., 2007).

## 2.2. Lagrangian particle tracking

The ANSYS Fluent CFD code was coupled to the DEM-Solutions EDEM (discrete element method) software via a coupling interface in order to predict the particle–laden flows of interest. What follows is a description of the various elements of this coupled approach used in the present work.

### 2.2.1. Governing equations

A Lagrangian approach was used to model particle motion from the instantaneous fluid velocity field in which the individual point particles are tracked along their trajectories through the unsteady, non-uniform flow field (Maxey and Riley, 1983; Gatignol, 1983). The particles can have two types of motion: translational and rotational. Their paths are computed based on Newton's second law for the translational and rotational accelerations. This is achieved by integrating the accelerations over a time-step, with particle velocities and positions updated. The rotational motion is calculated based on (13):

$$I\frac{d\omega}{dt} = \vec{M} \tag{13}$$

where $I$ is the moment of inertia, $\omega$ is the angular velocity, $t$ is time and $M$ is the resultant contact torque acting on the particle, defined as the product of the tangential contact force, $F_t$ and the particle radius, $R$. The translational motion is calculated based on (14):

$$m\frac{du_p}{dt} = F_g + F_c + F_{nc} \tag{14}$$

where $u_p$ is the translational velocity of the particle, $m$ is the mass of the particle, $F_g$ is the resultant gravitational force acting on the particle, and $F_c$ and $F_{nc}$ are the resultant contact and non-contact forces between the particle and surrounding media or walls, respectively. Fig. 1 gives a schematic representation of these forces for particles a and b, showing the resultant normal and tangential forces acting on the particles, $F_n$ and $F_t$, as well as the translational and angular velocities, where $\delta_n$ is the particle overlap, representing the deformation of the soft particles.

In this analysis, the aim was to minimise the number of degrees of freedom by keeping the simulations as simple as possible whilst still retaining the realism required for practical applications; thus all particles were assumed to be spherical with equal diameter and density, the effect of gravity was neglected, and particles were considered much heavier than the fluid ($\rho_p/\rho_f \gg 1$). This allows particle interaction with the flow structures alone to influence the particle motion. The work is thus aimed at elucidating the physics of

**Table 1**
Particle parameters used in the simulations.

| Surface energy/J m$^{-2}$ | $d_p$/μm | St($\tau_p^+$) | $\tau_p$/s | $\tau_f$/s |
|---|---|---|---|---|
| 0.0, 0.05, 0.5, 5.0 | 150 | 216 | 0.0612 | 0.000323 |

how turbulence influences the locations of particle interaction and agglomeration. This approach of omitting gravity in order to focus on the impact of particle–fluid interactions on particle motion in the flows examined has been adopted by various authors in the literature, e.g. Marchioli et al. (2008). The only significant force in such systems is the drag force, which has been justified by Armenio and Fiorotto (2001), with the buoyancy, added mass, pressure gradient and Basset forces negligible as they are an order of magnitude smaller for the density ratio used in the present study. Brownian motion of the particles was also not considered since the particle sizes are large enough ($d_p \geq 1\,\mu$m) to permit the neglect of this molecular effect. In coupling the fluid dynamic and particle motion, particle rotation due to fluid shear was also neglected on the grounds that this is only significant under high vorticity conditions. The shear induced Saffman lift force was taken in account as it has non-trivial magnitudes in the viscous sub-layer, with the large velocity gradients in such regions inducing pressure differences on the surface of the particle, causing lift. This work used a modified spherical, free-stream drag for calculation of the force on the particles. All fluid parameters are taken from the fluid computational cell which contained the centre of the DEM particle. This treatment is therefore only valid for particles of the same size as, or smaller than, a fluid control volume, or where the change in fluid parameters (e.g. velocity) over the extent of the particle remain approximately constant. The governing equation for a spherical particle is:

$$\frac{du_p}{dt} = 05C_D\rho_f A_p(u_f - u_p)|u_f - u_p| + \left(\frac{F_L}{m_p}\right) \tag{15}$$

where $u_f$ and $u_p$ are the fluid and particle velocity vectors, $\rho_f$ is the fluid density, $A_p$ is the projected particle area, and the lift force, $F_L$, was taken from Chaumeil and Crapper (2014). The corresponding drag coefficient $C_D$ depends on the particle Reynolds number $\mathrm{Re}_p$ given by Rowe and Enwood (1962):

$$C_D = \begin{cases} \dfrac{24}{Re_p} & Re_p \leq 0.5 \\ \dfrac{24}{Re_p}(1 + 0.15Re_p^{0.687}) & 0.5 \leq Re_p \leq 1000 \\ 0.44 & Re_p > 1000 \end{cases} \tag{16}$$

where

$$Re_p = \frac{\varepsilon\rho_f d_p|u_p - u_f|}{\nu} \tag{17}$$

and $d_p$ is the particle diameter, and $\varepsilon$ is the voidage/porosity of the fluid cell.

The various specifications for $C_D$ are required to extend the validity of the expression to cover a wide range of $\mathrm{Re}_p$, and in particular to accommodate depositing particles. The particles are characterised by the relaxation time, defined as $St = \Phi_\rho d_p^2/(18\nu)$, where $\Phi_\rho = \rho_p/\rho$ is the particle to fluid density ratio and $\nu$ is the fluid kinematic viscosity, and the non-dimensional particle response time is given by the particle Stokes number, $St = \tau_p^+ = \tau_p/\tau_f$, where $\tau_f$ is a characteristic time scale of the flow (defined as $\tau_f = \nu/u_\tau^2$). The shear velocity $u_\tau = 0.2335\,\mathrm{m\,s^{-1}}$ is obtained from the shear Reynolds number $\mathrm{Re}_\tau = hu_\tau/\nu$, given that $\mathrm{Re}_\tau = 300$, $h = 0.02$ m and $\nu = 1.57\times10{-}5\,\mathrm{m^2\,s^{-1}}$.

Three particle surface energies were considered, with the corresponding particle relaxation times, Stokes number and other relevant parameters given in Table 1. The range of implemented surface energies covers non-cohesive particles (0 J m$^{-2}$), cohesive particles such as those with van der Waals attraction (0.05 J m$^{-2}$), very cohesive materials, for example when liquid bridges form (0.5 J m$^{-2}$), and extremely cohesive particles (5 J m$^{-2}$). For the simulation results presented below, the particles considered are large with relaxation times greater than the smallest fluid time scales, therefore the influence of the unresolved scales in LES on particle motion are negligible (Pozorski and Apte, 2009).

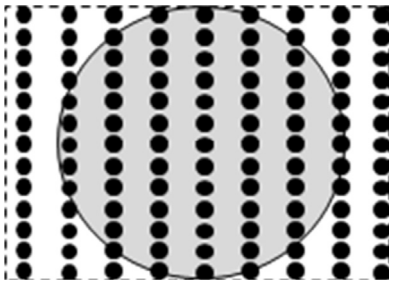

**Fig. 2.** Sample points within the volume surrounding a particle.

*2.2.2. Interaction: fluid forces on particle*

The instantanous fluid velocity $u_f$ required to solve Eq. (15) was obtained using tri-linear interpolation. It should also be noted that the particle time-steps required in solving their equation of motion are typically substantially smaller than the fluid time-steps in order to correctly capture any contact behaviour. The particles therefore do not move a significant distance in a single particle time-step. Typical ratios for the fluid:particle time-steps vary from 1:10 to 1:100. The fluid-particle coupling automatically adjusts the number of particle iterations carried out in order to match the fluid time-step.

*2.2.3. Interaction:particle forces on fluid*

The effect of particles on the continuous phase for volume fractions greater then $10^{-6}$ was taken into account, leading to a two-way coupled simulation as discussed earlier. The switch from one-way to two-way coupled regimes requires that the models used to calculate the drag and lift forces take into account the volume of particles found in each computational cell. The particle position is calculated at its centroid and its volume is returned as a scalar value. More detailed information about particle shape can also be calculated from the particle sample points. The representation of particle volume is based on multiple sample points, generated using the Monte–Carlo method. The method takes regular sample points within a box bounding a particle and keeps those points that lie within the particle's bounding surface, as illustrated in Fig. 2.

Each point is then checked to determine which fluid computational cell it lies within. The solid volume fraction within a particular cell is then the percentage of the number of sample points that lie within that cell, given by:

$$\varepsilon_s = 1 - \varepsilon = \sum_{\text{particles}} \frac{n_c}{N} V_p \tag{18}$$

where $n_c$ is the number of sample points contained within the cell of particle $p$, $N$ is the total number of sample points of the particle, and $V_p$ is the volume of the particle. Sample points are generated for each of the particle types defined in the simulation. Using the position, orientation and scaling of the individual particles, the precise coordinates for the points representing each particle can be calculated. Provided no additional particle types are later added to the simulation, sample points need only be collected once, at the start of a simulation. Particles have external forces applied to them before the LPT executes a simulation-step, and up-to-date

particle data are obtained and any force or torque applied to the particles during the simulation-step, prior to the LPT performing another simulation. Particle mass loading is considered through the momentum coupling terms of the continuous phase. The exchange of momentum between the two phases is achieved through the calculation of the momentum sink of the drag force that arises due to the relative velocity between the phases. An additional source term $f_i$ representing the forces exerted by the particles on the fluid is the added to the filtered Navier–Stokes Eq. (1). This momentum sink is calculated using:

$$f_i = \frac{\sum_i^n F_i}{V} \tag{19}$$

Hence, the sink term is the summation of the drag and lift forces, $F_i$, which are exerted on the fluid in that fluid cell, and $V$ is the volume of the fluid solver finite-volume cell.

A smooth source term distribution is achieved by using a trilinear distribution of the contribution of the particles to the eight finite-volume cell centres surrounding the particle. Any further interactions between the phases are neglected, e.g. possible influences of the particles on the sub-grid scale stresses of the fluid are not taken into account. The reason for this is that when particle motion is computed using a well resolved LES velocity field, the approach is accurate for simulating gas–solid turbulent flow without any modelling of the sub-grid fluid velocity in the particle trajectory equation (Armenio et al., 1999). The sub-grid fluid turbulence scales will also hardly affect the instantaneous particle motion, and will have even less of an effect on the statistical properties, such as the mean particle concentration and the root-mean square of the particle velocity fluctutations (Kuerten, 2006). This is particularly the case for large particles (i.e. the 150 μm particles considered herein) in low and moderate Reynolds number flow ($Re_\tau = 300$).

### 2.2.4. Interaction: particle forces on particle

At particle volume fractions greater than $10^{-3}$ the flow is no longer considered to be a dilute dispersed two-phase flow (Laín and Sommerfeld, 2008). In such flows, particle–particle collisions play an important role and must be accounted for, with this being commonly referred to as four-way coupling. One exception is for flows that include particles of large Stokes number ($St > 100$), where for volume fractions less than $10^{-3}$ particle accumulation in the near-wall region is common and results in a considerable number of particle–particle interactions. In this work, the particle–laden flow was dilute (particle volume fraction $\sim 10^{-5}$), and the prediction method incorporated full coupling between the phases, i.e. interactions between particles were considered, and the flow and particles were two-way coupled. particle–wall collisions were assumed to be inelastic, with the Poisson's ratio, shear modulus, and coefficient of restitution set to 0.25, $1 \times 10^7$ Pa and 0.5, respectively. The coefficient of restitution selected is a realistic value associated with many compounds found in nature, for example calcium carbonate which can form limescale due to deposition (see Mangwandi et al., 2007). particle–particle interactions were modelled using the discrete element method incorporating the Hertz–Mindlin contact model with Johnson–Kendall–Roberts (JKR) cohesion to allow the simulation of van der Waals forces which influence the particle behaviour (Johnson et al., 1971). This approach only considers the attractive forces within the contact area, i.e. the attractive inter-particle forces are of infinite short range. JKR builds on the conventional Hertz model by incorporating an energy balance to extend it to cover two elastic-adhesive spheres. The contact area predicted by the JKR model is larger than that given by the Hertz model; this creates an outer annulus in the contact area which experiences tensile stress. This annulus surrounds an inner circular region over which a Hertzian compressive distribution acts (Thornton and Yin, 1991). When two spheres come into contact, the normal force between them immediately drops to a certain value (8/9 $f_c$, where $f_c$ is the pull-off force (Thornton and Ning, 1998)) due to van der Waals attractive forces. The velocity of the spheres gradually reduces and some of the initial kinetic energy is radiated into the substrate as elastic waves. The loading stage is complete when the contact force reaches a maximum value and particle velocity drops to zero. In the recovery stage, the stored elastic energy is released and converted into kinetic energy causing the spheres to move in opposite directions. All the work done during the loading stage has been recovered when the contact overlap becomes zero. At this stage, however, the spheres remain adhered to each other and further work (known as work of cohesion) is required to separate the surfaces. The contact breaks at a negative overlap, $\alpha_f$, for a contact force 5/9 $f_c$ (Ning, 1995). The pull-off force is the maximum tensile force the contact experiences and is given by (Johnson et al., 1971):

$$f_c = \frac{3}{2}\pi R^* \Gamma \tag{20}$$

where $\Gamma$ is the surface energy per unit area and $R^*$ is the equivalent radius defined as,

$$R^* = \frac{R_1 R_2}{R_1 + R_2} \tag{21}$$

where $R$ is the particle radius, with the subscripts 1 and 2 representing the interacting particles 1 and 2. The governing equation for the force-overlap is given by (Johnson, 1985):

$$F_n = \frac{4E^* a^3}{3R^*} - (8\pi\Gamma E^* a^3)^{1/2} \tag{22}$$

where $a$ is the radius of overlap and $E^*$ is the equivalent Young's modulus defined as,

$$E^* = \left(\frac{1-\upsilon_1^2}{E_1} + \frac{1-\upsilon_2^2}{E_2}\right)^{-1} \tag{23}$$

for $\upsilon$ the Poisson's ratio, and $E$ the Young's modulus of elasticity ($E = 2G(1+\upsilon)$), and where $G$ is the shear modulus. The overlap $\alpha$ can be evaluated by (Johnson, 1985):

$$\alpha = \frac{a^2}{R^*} - \left(\frac{2\pi\Gamma a}{E^*}\right)^{1/2} \tag{24}$$

The particle surface attractive force was altered by specifying the interface energy, with the amount of interface energy influencing the cohesion of the particles. In this analysis, the aim was to minimise the number of degrees of freedom by keeping the simulation settings as simplified as possible; thus all particles were assumed to be rigid spheres with equal diameter and density, the effect of gravity was neglected, and particles were assumed to be much denser than the fluid, as already noted.

The particles are treated as distinct elements which displace independently from one another and interact only at point contacts (Cundall and Strack, 1979). Particle motion in regions of high particle number density is affected not only by the forces and torques originating from contacts with its immediate neighbouring particles, but also by disturbances propagating from more distant particles. To avoid evaluation of the effects of disturbance waves, the combined DEM-LPT approach integrates fluid hydrodynamic forces and torques into the particle simulation on an individual particle level. When the DEM-LPT performs a time-step of the simulation, the external forces act upon the particles in addition to any collision forces. Fig. 3 depicts the various stages of the DEM-LPT simulation loop and the point at which it interacts with the LES solver. As a result, any disturbance cannot propagate from each particle further than its immediate neighbouring particles (Cundall and Strack, 1979). The speed of disturbance waves may

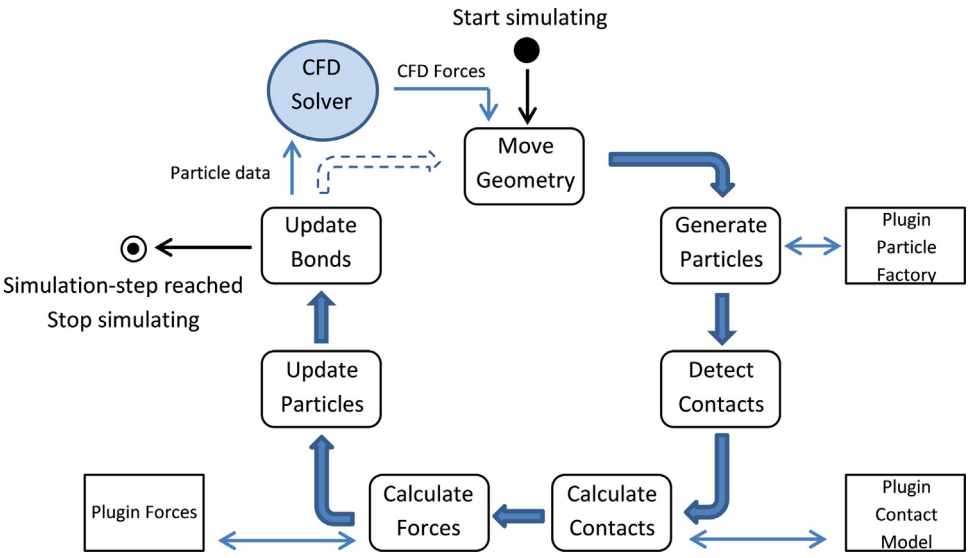


**Fig. 3.** The LES-DEM-LPT solution cycle (based on DEM-Solutions, 2013).

be approximated by Rayleigh surface wave propagation based on the physical properties of the discrete medium. The time-step used must be sufficiently smaller than the Rayleigh time-step in order to ensure realistic force transmission rates in the particle assembly and to prevent numerical instability (Ning and Ghadiri, 2006). The Rayleigh time-step is given by:

$$T_R = \frac{\pi R\left(\frac{\rho}{G}\right)^{1/2}}{0.16361\upsilon + 0.8766} \tag{25}$$

where $R$ is the particle radius, $\rho$ is the density, $G$ is the shear modulus and $\upsilon$ is Poisson's ratio for the particle. In practice, some fraction of this maximum value is used for the integration time-step. For dense systems (coordination numbers $\geq$4) a typical time-step of 0.2 $T_R$ has been shown to be appropriate and for less dense systems 0.4 $T_R$ is more suitable. In this work a time-step of 0.2 $T_R$ was selected. Since the time-step varies with different particle materials, for an assembly consisting of particles of different material types, the critical time-step should in general be the smallest among those determined for the different material properties.

During a coupled LES-DEM-LPT calculation (Fig. 3), the LES solver and the DEM-LPT simulate in an alternating manner, with the LES solver first creating a fluid flow field into which particles are introduced. The LES solver simulates ahead in time and resolves the flow field of the continuous phase. When a stable solution is obtained, the flow field is passed to the coupling module, where the relative velocity between each particle and the surrounding fluid is calculated in order to obtain the drag force. The drag and lift forces acting on each particle are then passed to the DEM solver which updates the particle positions in a loop, until the end of the LES time-step is reached. The new particle positions are then handed back to the coupling module, which then updates the fluid cell porosities and calculates the momentum sink term for each cell. Based on this input, the LES solver iterates over the next time-step until the flow field again converges to a stable solution (Di Renzo et al., 2011; Favier et al., 2009). This alternating pattern continues until the simulation time has reached the specified end time, as shown in Fig. 4. Due to the explicit time integration methods implemented in DEM it is common that multiple time-steps are required to simulate the same time period as a single time-step of an LES simulation. Therefore, the time-steps used in the two solvers are potentially different; however the simulation-steps are the same.

Each time the LES coupling interface sends a message to the DEM-LPT it blocks any further messages from being sent until the DEM-LPT returns a response. This synchronous behaviour effectively pauses the LES solver until the DEM-LPT has calculated the required simulation step. The sequence of a coupled simulation is shown in Fig. 5, with the LES coupling interface relaying information on fluid forces and particle data between the two solvers. Once a coupling is successfully initialised between the DEM-LPT and the LES solver, the DEM-LPT is ready to start simulating (Steps 1–3). Simulation in the DEM-LPT commences when the LES solver sends fluid forces to apply to the particles in the simulation (Steps 5, 7, 9).

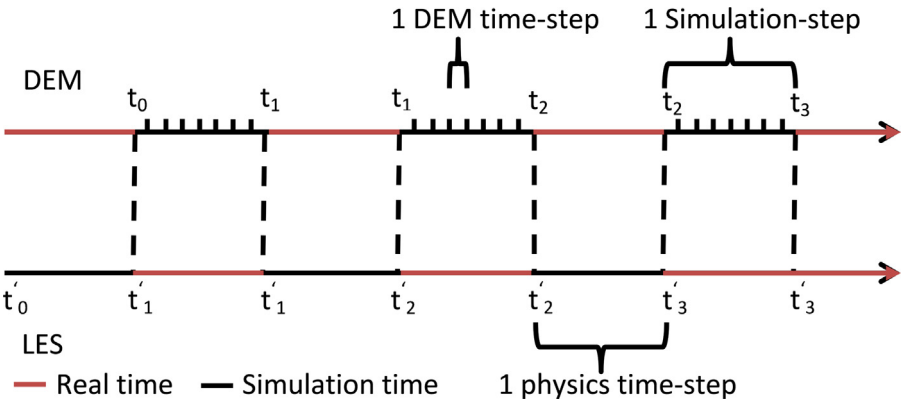


**Fig. 4.** The alternating sequence of a coupled simulation (based on DEM-Solutions, 2013).

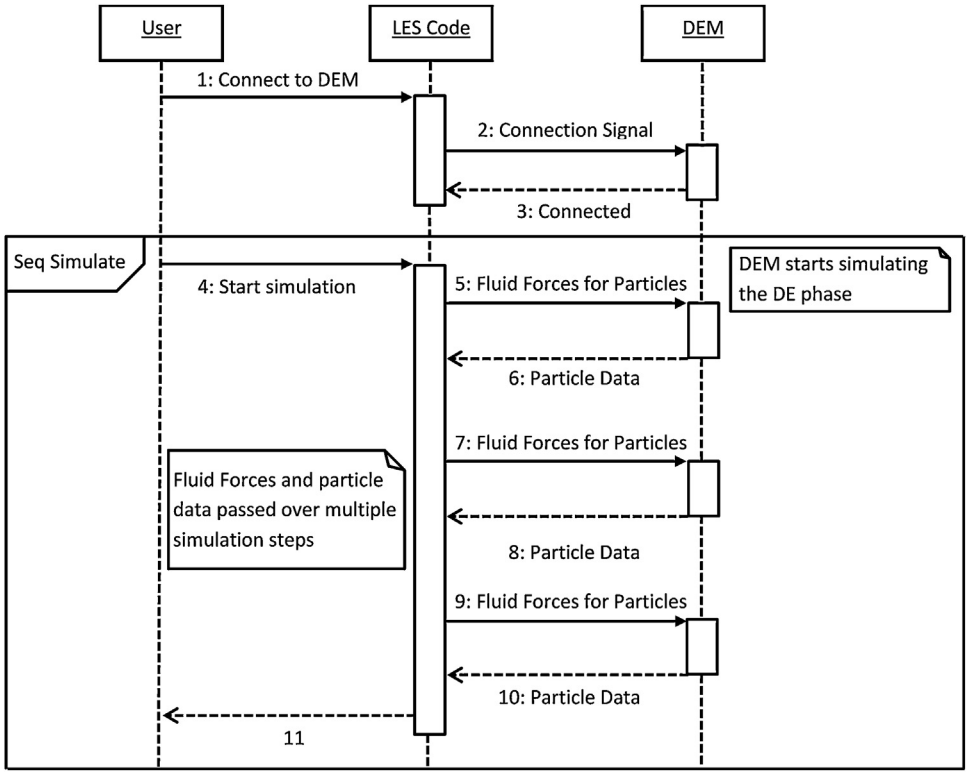


**Fig. 5.** The coupled simulation sequence (based on DEM-Solutions, 2013).

If this is the first step of a simulation, and there are no particles to apply forces to, then this can be omitted before starting the LES-LPT simulation-step. After the DEM-LPT completes the simulation-step, it is possible to retrieve the new or updated particle information from the simulation. This information is then returned to the LES solver (Steps 6, 8, 10) in order to update the solver's variables and advance the simulation.

## 3. Results and discussion

### 3.1. Flow configuration

The flow into which particles were introduced was a turbulent channel flow of gas; Fig. 6 gives a schematic diagram of the channel geometry and co-ordinate system. The flow is described by a three-dimensional Cartesian co-ordinate system ($x$, $y$ and $z$) representing the streamwise, spanwise and wall-normal directions, respectively. The boundary conditions for the momentum equations were set to no-slip at the channel walls and the instantaneous flow field was considered to be periodic along the streamwise and spanwise directions, with a constant mass flux through the channel in the streamwise direction maintained by a dynamically adjusted pressure gradient used to drive the flow. The shear Reynolds number, $Re_\tau = hu_\tau/\nu$, used in the simulations was 300, corresponding to a bulk Reynolds number $Re_b \sim 8400$.

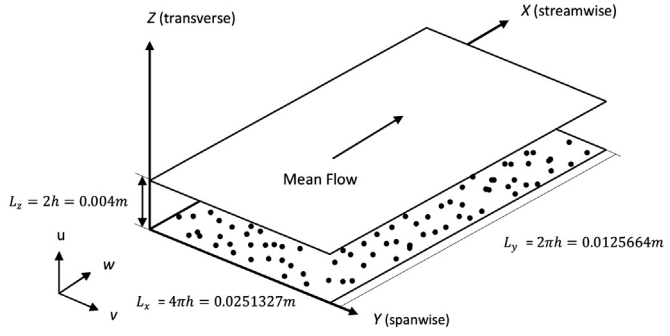


**Fig. 6.** Schematic diagram of the channel geometry and co-ordinate system.

The rectangular channel considered was of dimensions $2h \times 2\pi h \times 4\pi h$, which in terms of wall units corresponds to $L_x^+ = 3770$, $L_y^+ = 1885$ and $L_z^+ = 600$. The length of the channel in the streamwise direction was sufficiently long to capture the streamwise-elongated, near-wall turbulent structures that exist in wall-bounded shear flows; such structures are usually shorter than ~1000 wall units (Robinson, 1991). Sensitivity studies were carried out using different numerical grid distributions and numbers of computational nodes (minimum grid size limited by particle size), and for the final grid arrangements, selected turbulence statistics were found to be independent of grid resolution. Based on the uniform Cartesian grid employed, $81 \times 80 \times 80$, the grid resolution was $\Delta z^+ = 9.23$ and $\Delta y^+ = 29.45$ wall units in the wall-normal and spanwise directions, respectively, and $\Delta x^+ = 58.90$ in the streamwise direction. A second simulation using an increased total number of non-uniformly distributed nodes was also used to give better resolution near the floor of the channel. This used a minimum grid resolution of $\Delta z^+ = 2.4$ and $\Delta y^+ = 14.73$ wall units in the wall-normal and spanwise directions, respectively, and $\Delta x^+ = 29.45$ in the streamwise direction. To save computational effort, the coarse grid was employed for general analysis, with the more refined simulation used to give detailed flow information near the wall boundary. The dimensional integration time-step used for the fluid and particles was $\Delta t = 1.0 \times 10^{-5}$ and $5.2 \times 10^{-7}$ s, respectively.

The initial particle positions were distributed randomly throughout the channel, corresponding to an initially uniform wall-normal particle number density profile. The initial particle velocity was set to zero, with the particles gradually coming in-line with local fluid velocities with time. Particles were assumed to interact with turbulent eddies over a certain period of time, that being the

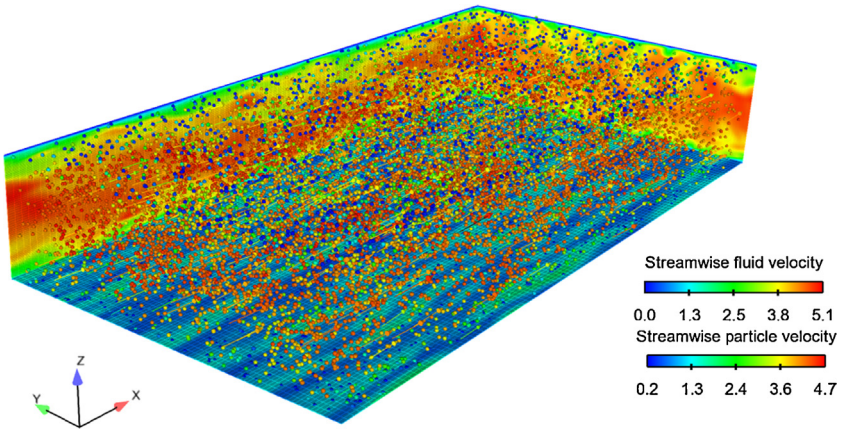


**Fig. 7.** Contour plot of the instantaneous streamwise velocity for both the fluid and particle phase, in m s$^{-1}$.

lesser of the eddy lifetime and the transition time. Particles that moved out of the rectangular channel in the streamwise and spanwise directions were re-introduced back into the computational domain using periodic boundary conditions. The total number of particles considered in the computational domain was 20,000 in all cases. Particle and fluid densities were set to $\rho_p = 1000\,\mathrm{kg\,m^{-3}}$ and $\rho_f = 1.3\,\mathrm{kg\,m^{-3}}$, respectively, with the kinematic viscosity set to $\nu = 15.7 \times 10^{-6}\,\mathrm{m^2\,s^{-1}}$.

### 3.2. Flow field simulations

An example of the instantaneous streamwise velocity contours for both the fluid and particles predicted by the LES is given in Fig. 7. The velocity is seen to be at a maximum in the centre of the channel and decreases to a minimum towards the walls, due to the no-slip boundary conditions applied there. Fig. 8a shows a contour plot of the mean streamwise fluid velocity, whilst Fig. 8b gives a contour plot of the root-mean-square (rms) of the streamwise velocity fluctuation, the values of which are seen to be a minimum at the walls and increase to a maximum just away from the wall, decreasing to a lower value towards the channel centre.

The results generated by the LES for the fluid phase were validated using DNS predictions (Marchioli et al., 2008) for a shear Reynolds flow of $Re_\tau = 300$. Wall-bounded turbulent flows comprise a number of regions, each with distinct flow characteristics, although frequently the flow is divided into an inner and outer layer. The inner layer encompasses the near-wall region, wherein the flow is considered to be unaffected by the geometry of the system. This means that flow quantities in the inner layer are alike in spite of the type of flow geometry (e.g. channel, duct or pipe). The outer layer, conversely, is dependent on the flow geometry. To make quantitative comparison between the LES and DNS results, the flow solutions provided by both were scaled. For a smooth wall, suitable scaling parameters for the inner layer include the kinematic viscosity $\nu$, and the friction velocity $u_\tau$ (defined as $u_\tau = (\tau_w/\rho)^{1/2}$), where $\tau_w$ is the mean shear stress at the wall and $\rho$ is the fluid density. Inner layer scaling then demands that the relationship given below holds for the mean streamwise fluid velocity, $U_x$:

$$U_x^+ = f(z^+) = U_x/u_\tau \tag{26}$$

where $U_x^+$ is the non-dimensional mean streamwise fluid velocity, $f$ is a universal function (independent of Reynolds number) and $z^+$ is the dimensionless distance from the wall. All variables reported below are in dimensionless form, represented by the superscript (+), and expressed in wall units, with the latter obtained by combining with $u_\tau$, $\nu$ and $\rho$.

The mean velocity profile in a turbulent channel flow at high Reynolds number in the inner and outer layers may be represented using the expressions given by Von Karman (1930):

$$U_x^+ = z^+, \quad \text{for} \quad 0 < z^+ < 5 \tag{27}$$

$$U_x^+ = A \ln z^+ + B, \quad \text{for} \quad z^+ > 30 \tag{28}$$

The above equations represent the analytical mean velocity profile given by the law of the wall, (27), and by the log-law, (28). The value of the constants A and B is an area of dispute due to the large amount of scatter in values derived from experimental measurements. For fully developed flow at high Reynolds numbers, however, the average of all experimental data suggests that $A = 2.5$ and $B = 5.0$ (Kim et al., 1987).

Fig. 9a shows the mean streamwise fluid velocity profile, $U_x^+$, plotted in semi-logarithimic form as predicted by the LES, together with DNS results and the analytical profiles. The LES results show the anticipated symmetric behaviour for a fully developed flow and

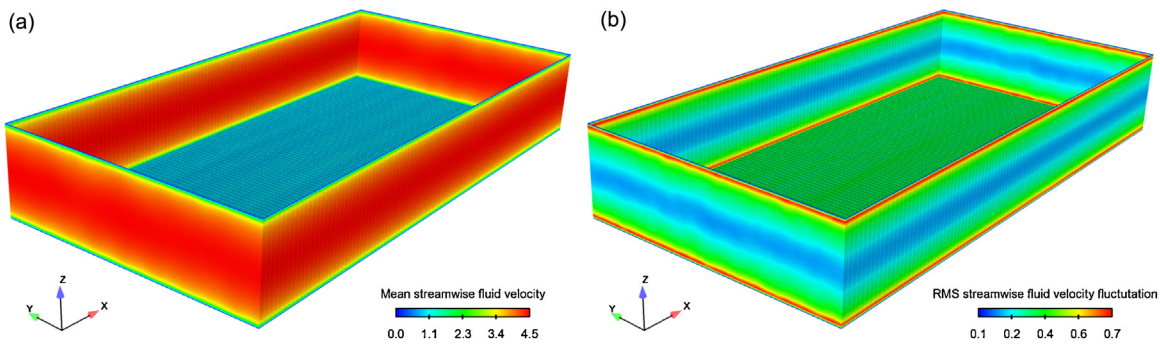


**Fig. 8.** Contour plots of (a) the mean streamwise velocity, and (b) the rms of the streamwise velocity fluctuation, in m s$^{-1}$.

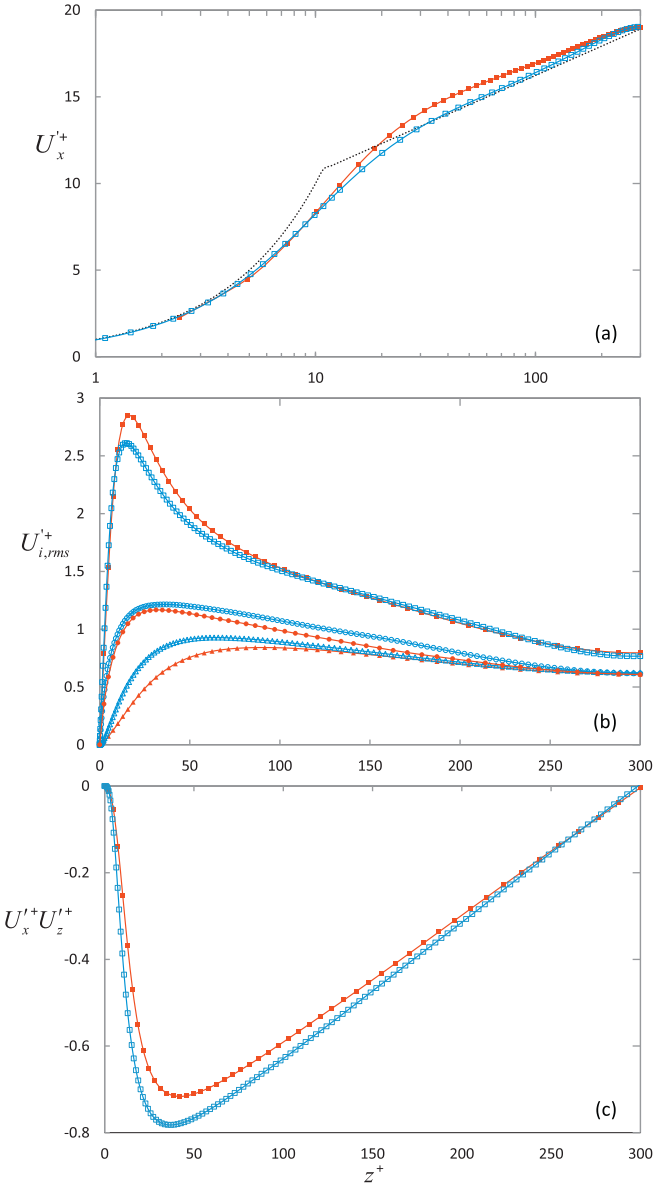


**Fig. 9.** (a) Mean streamwise fluid velocity (—■— LES; —□— DNS; ···· analytical profiles); (b) root-mean-square of fluid velocity fluctuations (red symbols – LES, blue symbols – DNS; —■— $U'^+_{x,\mathrm{rms}}$; —●— $U'^+_{y,\mathrm{rms}}$; —▲— $U'^+_{z,\mathrm{rms}}$); and (c) Reynolds stress component (—■— LES; —□— DNS). (For interpretation of the references to colour in this figure legend, the reader is referred to the web version of this article.)

follow the general trend of the DNS, providing reasonable agreement overall. The LES clearly predicts the viscous sub-layer to a high degree of accuracy and quantitatively tends towards (27) as this region is approached. In the buffer layer, the flow is predominantly characterised by small-scale turbulence, as modelled by the SGS model. Good agreement with DNS results in this region is therefore indicative of the accuracy of the SGS model. It is seen that the LES slightly over predicts the DNS in this region, although the log scale used emphasises any discrepancies close to the wall and therefore highlights any differences. The logarithmic law given by (28) is shown for the region $z^+ > 30$, based on the values suggested by Kim et al. (1987), with the LES results seen to over predict this analytical profile and the DNS results, although the various approaches come in line at the centre of the channel. In this region of the channel, the flow characteristics are dominated by large energetic scales of motion and, given that these scales are directly computed by the

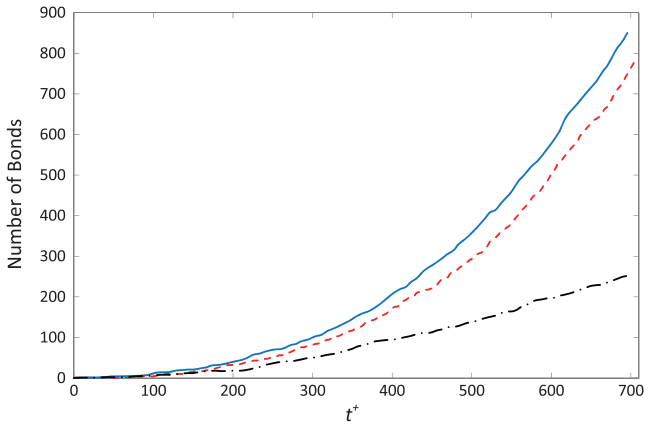


**Fig. 10.** Variation of number of bonds between particles with time (•—•, ▬▬, ▬ surface energies of 0.05, 0.5 and 5.0 J m$^{-2}$, respectively). (For interpretation of the references to color in this figure legend, the reader is referred to the web version of this article.)

LES, the predicted profile should match the DNS, with the differences observed due to the lack of resolution in the LES. Overall, however, the streamwise mean velocity generated by the LES is in acceptable agreement with the DNS.

Fig. 9b gives the rms of the non-dimensional fluid velocity fluctuation ($U'^+_{i,\mathrm{rms}}$) in the streamwise, spanwise and wall-normal directions. Results are in good agreement with the DNS for the $U'^+_{x,\mathrm{rms}}$ component, with the positions of the peak and minimum values of this profile at the channel centre predicted well. Further scrutiny of the results, however, shows an over prediction in the region $10 < z^+ < 106$, with the discrepancy being greater in regions of higher turbulence. The $U'^+_{y,\mathrm{rms}}$ and $U'^+_{z,\mathrm{rms}}$ profiles also follow the trend of the DNS, although qualitative and quantitative differences are observed in some regions. For $U'^+_{y,\mathrm{rms}}$, an under prediction by the LES increases from the buffer layer into the log region where it reaches a maximum before decreasing towards the channel centre. For $U'^+_{z,\mathrm{rms}}$, this difference increases from the wall and throughout the viscous sub-layer region into the buffer layer where it reaches a maximum, before decreasing towards the outer layer. Agreement between the LES and DNS in the channel centre is good for all the profiles given in Fig. 9b and close to the wall for $U'^+_{x,\mathrm{rms}}$ and $U'^+_{y,\mathrm{rms}}$. Lastly, Fig. 9c shows the time-averaged $U_x'^+U_z'^+$ component of the Reynolds stress tensor. Again, the LES profile follows that of the DNS and predicts the location of the minimum in the profile with good accuracy. Quantitatively, the buffer layer and log-law region DNS results are slightly under predicted, with this discrepancy being largest at the peak in the profile.

Overall, agreement between the LES and DNS results of Marchioli et al. (2008) is satisfactory, with this study confirming that the proposed simulation approach faithfully captures the turbulent velocity field within the channel flow. Extension of the simulations to include particles should therefore produce reliable predictions for the particle–laden flows of interest.

### 3.3. Particle bond formation

Fig. 10 shows results for the number of particle bonds in the channel. The results clearly illustrate a general increase in the number of bonds with time due to the effects of fluid turbulence in causing particle collisions; furthermore, the rate at which the particles form bonds increases with the particle surface energy, as would be anticipated. For the 0.05 J m$^{-2}$ surface energy particles the rate of bond formation increases roughly linearly with time after an initial period. In the higher surface energy cases, however, the trend is exponential, indicating an ever increasing rate at which particle

bonds form with time. Further scrutiny of the results, for all the particles, shows that agglomeration is first seen to occur at around $t^+ = 53$; here the particles have increased their velocity to an extent where the fluid turbulence causes particle–particle interactions. A linear increase in particle bond numbers then continues to about $t^+ = 300$, after which an increasing divergence is seen between the higher (5.0 and 0.5 J m$^{-2}$) and the lower (0.05 J m$^{-2}$) surface energy particles. This behaviour suggests that there is some phenomenon taking place within the channel that advantages the higher surface energy particles in the formation of agglomerates, other than the surface energy alone. This occurs as a result of regions of high particle concentration and low particle velocity near the channel walls; in such regions the number of bonds formed can be proportionally higher for particles of greater surface energy as the particle kinetic energy is sufficiently low to be ineffective in preventing particle separation after collision. Further detailed analysis is required in order to establish a firm relationship between particle surface energy and kinetic energy, and their impact on the formation of successful bonds. The dispersing behaviour of the particles and the regions in which particle bonds are formed is, however, discussed further below. At the end of the simulation ($t^+ \approx 696$), and for the 0.05, 0.5 and 5.0 J m$^{-2}$ surface energy particles, respectively, there are 252, 750 and 850 particle bonds in the flow. The greater surface energy of the 0.5 J m$^{-2}$ particles compared to the 0.05 J m$^{-2}$ particles, by one order of magnitude, therefore gives rise to more than three times the number of bonds. However, a further increase of one order of magnitude in the surface energy to 5.0 J m$^{-2}$ does not result in an equivalent increase in the number of bonds. This is indicative of the surface charge value nearing a threshold beyond which any further increase does not dramatically enhance particle agglomeration. From the above analysis, it is clear that the effects of fluid turbulence are dominant in creating particle–particle interactions, and that the particle surface energy is likewise a key factor in determining particle agglomeration in the flow.

### 3.4. Particle agglomerate formation

Fig. 11a–c shows the time dependent number of particles within the agglomerates, for all particle surface energies considered. In general, the number of single particles decreases gradually with time as the number of agglomerates increase within the simulation. For the single particles, there are initially 20,000, but this value begins to decrease at approximately $t^+ = 53$ in all cases and then follows a rapidly decreasing trend to 19,424 (for the 0.05 J m$^{-2}$ surface energy particles), 18,614 (0.5 J m$^{-2}$) and 18,391 (5.0 J m$^{-2}$) at $t^+ \approx 696$. It is clear that the rate of decline of the single particles increases with surface energy. The number of agglomerates is also inversely proportional to the number of single particles, with these agglomerates forming first at $t^+ = 53$ and increasing in number to final values of 260, 638 and 738 for the low, medium and high surface energy particles, respectively, at $t^+ \approx 696$. In all cases the majority of the agglomerates are also duplets. For the low surface energy particles the triple and quadruple particle agglomerates first appear at $t^+ = 371$ and 654, although there are only 3 and 0 present in the channel, respectively, at the end of simulation due to particle agglomeration and breakage. The medium surface energy particles first form triple, quadruple and quintuple agglomerates at $t^+ = 300$, 371 and 477, which increase to values of 30, 12 and 1 over the course of the simulation. Lastly, for the high surface energy particles the triple, quadruple, quintuple and sextuple particle agglomerates first appear at $t^+ = 371$, 371, 581 and 654 and finish with values of 41, 10, 5 and 0 at $t^+ \approx 696$. Over the simulation time considered, there are always far more double particles as compared to triple and larger agglomerates, and this difference was seen to increase further with time, with a longer simulation time clearly required before significant numbers of triple and larger particle agglomerates can be formed. Moreover, the higher surface energy particles show a greater propensity to form larger agglomerates in the time frame considered, as might be anticipated. This indicates that the stronger bonds between higher surface energy particles are more resistant to the effects of fluid drag, allowing larger particle chains to form in the system. Based on these trends, it is clear that with time the number of agglomerates, and the size of the agglomerates, will continue to increase, and that this will be greatest for the higher surface energy particles.

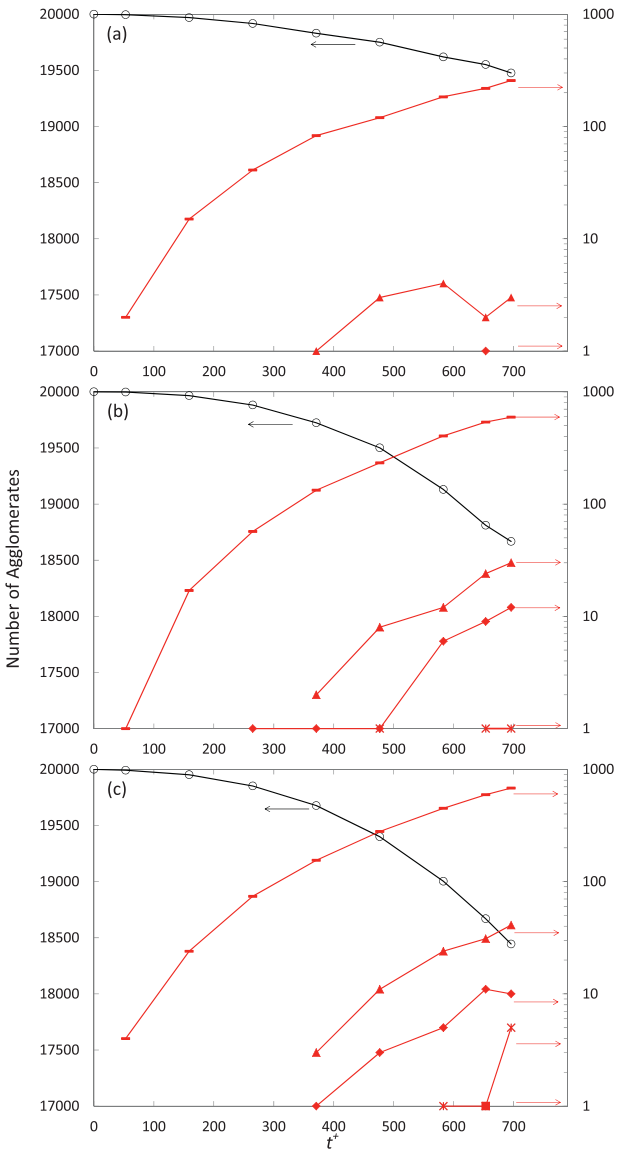


**Fig. 11.** Variation of number of particle agglomerates with time for surface energies of (a) 0.05 J m$^{-2}$; (b) 0.5 J m$^{-2}$; and (c) 5 J m$^{-2}$ (—○—, ▬▬▬, —▲—, ▬▲▬, ▬♦▬, —■— single, double, triple, quadruple, quintuple, and sextuple agglomerates, respectively). (For interpretation of the references to colour in this figure legend, the reader is referred to the web version of this article.)

Fig. 12 shows the relationship between the instantaneous position of the particles and agglomerates in the wall-normal direction for all three particle surface energies, and their number in this direction at $t^+ = 265$, 477 and 689. Results are shown for eight equally spaced regions across half the channel height, with particle statistics combined within each of the regions of fluid considered. The location of each

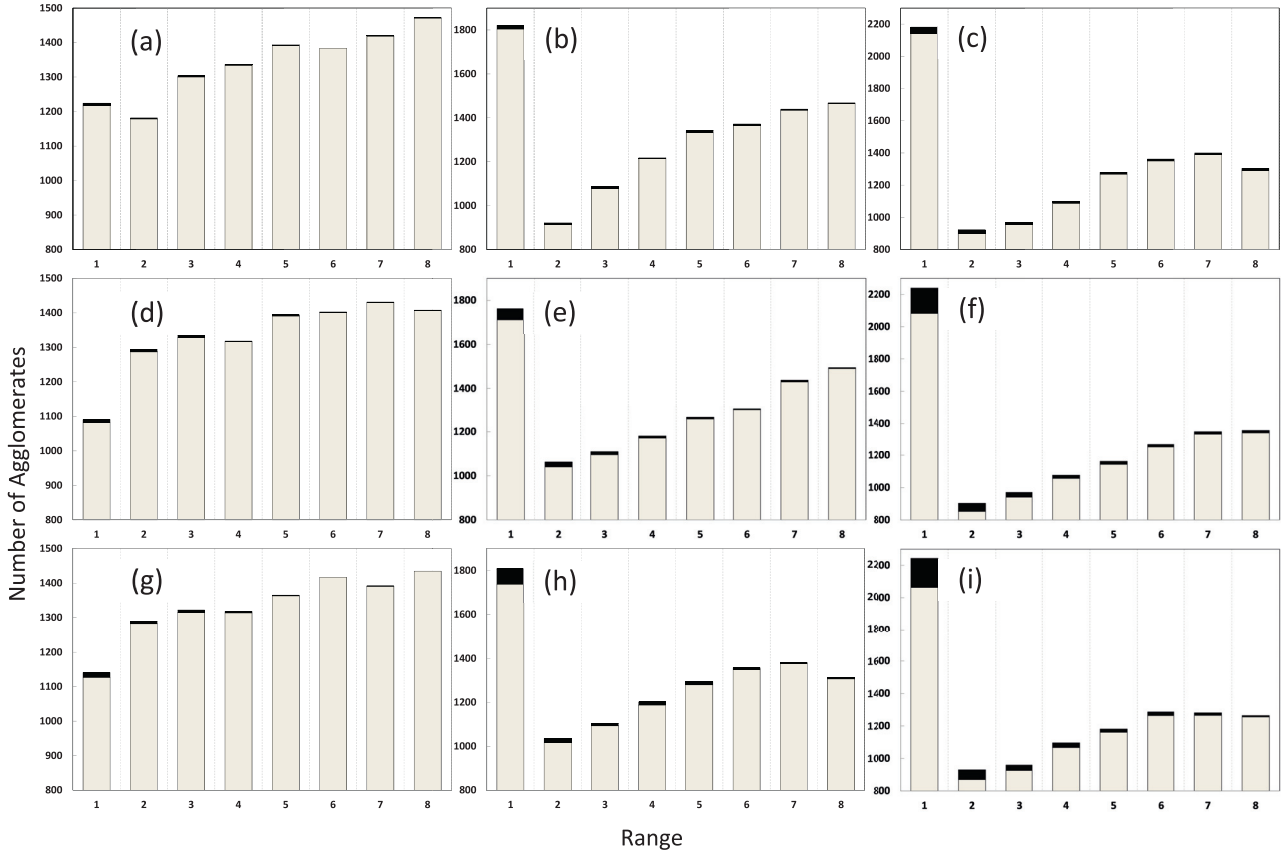


**Fig. 12.** Agglomerate number distribution across the channel for 0.05 J m$^{-2}$ surface energy particles at (a) $t^+ = 265$; (b) $t^+ = 477$; and (c) $t^+ = 689$, for 0.5 J m$^{-2}$ at (d) $t^+ = 265$; (e) $t^+ = 477$; and (f) $t^+ = 689$, and for 5 J m$^{-2}$ at (g) $t^+ = 265$; (h) $t^+ = 477$; and (i) $t^+ = 689$ (□ single, ■double-sextuple agglomerates).

region of fluid is represented by a column and plotted in relation to the channel walls, where column 1 is the region adjacent to the upper and lower walls; these particular regions have a width that stretches over 38 wall units covering the viscous sublayer ($y^+ < 5$) and the buffer layer ($5 < y^+ < 30$) within the near-wall region.

The results show a general movement of particles and agglomerates (or particle count) towards the walls with time, indicated by column 1 which accounts for over 1/5th of the total particle count by $t^+ = 689$. Closer examination of the results reveals two opposing trends; a steady decrease in particle number from the centre of the channel (column 8) towards the walls up to and including region 2, followed by a dramatic increase in particle count adjacent to the walls. This indicates that particle numbers at the walls are directly related to the momentum of the particles prior to wall impact, such that higher velocity particles located in the centre of the channel move towards the walls but rebound off them with a high velocity, then travelling back into the central region of the channel. In contrast, particles that move towards the walls with a lower velocity have less momentum and after impact with the wall become entrained in the near-wall region.

Focusing on the agglomerates, the results clearly show an increase in their number towards the walls of the channel with time. For the lowest surface energy particles, at the channel centre, the fraction of the number of agglomerates to the total particle count is 0.00, 0.002, and 0.01 for times $t^+ = 265$, 477 and 689, respectively, although these values are seen to increase towards the walls, where for the regions adjacent to the wall they increase to 0.005, 0.009 and 0.018. For the medium surface energy particles, at the channel centre, the fraction of the number of agglomerates to the total particle count is 0.00, 0.003 and 0.012 for times $t^+ = 265$, 477 and 689, respectively, and for region 1 this value increases to 0.008, 0.028 and 0.066. When compared with the 0.05 J m$^{-2}$ particles, the latter values are slightly higher at the channel centre and significantly higher at the walls. Lastly, for the highest surface energy particles, at the channel centre the fraction of the number of agglomerates to the total particle count is 0.00, 0.0038 and 0.007 for times $t^+ = 265$, 477 and 689, respectively, with these values similar to those observed for the 0.5 J m$^{-2}$ particles. However, the rate of increase in the number of agglomerates close to the walls is seen to be higher; in region 1 these values are 0.013, 0.038 and 0.074 at the times noted.

The number of agglomerates also increases uniformly towards the walls, in contrast to the total number count, with the exception of the final near-wall regions where significantly increased numbers are found. Therefore, depending on the location of the agglomerates relative to the wall, two different mechanisms are responsible for their formation. Particle agglomeration near to the wall is therefore attributable to the high particle concentration in these regions, with the regions closest to the walls showing the highest particle count and number of agglomerates. In the remaining regions, particle agglomeration is enhanced in high fluctuating fluid velocity fields which lead to a high number of particle–particle interactions. These velocity fluctuations are typically at a maximum 30 wall units away from the solid boundaries. This influence is indicated by the results for region 2, which contains the lowest particle count and yet the highest agglomerate number (bar those regions closest to the walls).

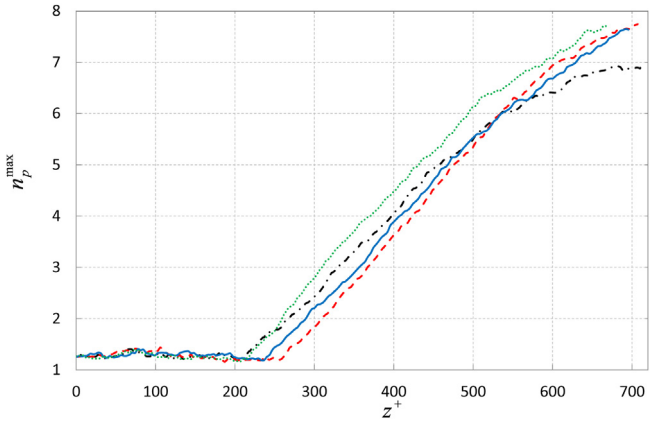


**Fig. 13.** Maximum particle number density at the wall as a function of time (••••, •—•, ▬▬, ▬ surface energies of 0.0, 0.05, 0.5 and 5.0 J m$^{-2}$, respectively). (For interpretation of the references to colour in this figure legend, the reader is referred to the web version of this article.)

### 3.5. Particle dispersion and turbophoretic drift

Fig. 13 shows the time evolution of the maximum value of the particle number density, $n_p^{max}$, close to the channel walls. The rationale for monitoring this quantity lies in the fact that the concentration close to the wall takes the longest time to reach a steady state. The results clearly show that, starting from an initial distribution corresponding to a flat profile centred around $n_p^{max} = 1$, from $t^+ = 216$–$265$ the particles accumulate at the walls at an approximately linear rate. From earlier work, it is known that for turbulent channel flows particle locations close to a wall correlate with instantaneous regions of low velocity along the streamwise direction, with the particles avoiding regions of high velocity, with the former defined as areas of lower-than-mean streamwise velocity (Pan and Banerjee, 1996). The behaviour demonstrated in Fig. 13 is consistent with the findings reported by Marchioli et al. (2008) for flow in a channel, where turbophoresis causes the accumulation of particles in near-wall regions, which in the present flow clearly also enhances the rate of particle agglomeration in such regions.

## 4. Conclusions

The work described in this paper was undertaken to gain insight into fundamental aspects of turbulent gas–particle flows. In particular, the effect of particle surface energy and fluid turbulence on particle agglomeration for turbulent flow in a channel was investigated. The mathematical modelling technique used was based on the large eddy simulation approach embodied in the commercial CFD code FLUENT, with flow solutions provided by this method coupled to a second commercial code, EDEM, based on the discrete element method and used for the prediction of particle motion and interaction.

The results generated by LES for the fluid phase have been validated against direct numerical simulations of a channel flow with a shear Reynolds number, $Re_\tau = 300$. Overall, the LES shows good agreement with the latter results, with mean velocities and normal and shear stresses matching those of the DNS to an acceptable level. Although not considered herein, the $Re_\tau = 300$ flow was also used to further investigate particle phase behaviour, with predictions again successfully validated against one-way coupled DNS results.

Further work considered the prediction of those conditions favouring particle aggregation and dispersion within a turbulent channel flow. Particles with identical physical parameters were simulated with three different surface energies using the fully coupled LES-DEM approach. The results derived show that the turbulent structure of the flow dominates the motion of the particles creating particle–particle interactions, with a positive relationship between particle surface energy and agglomeration observed. The process of particle agglomeration was found to be enhanced in two separate regions within the channel; in the near-wall region due to the high particle concentration there driven by turbophoresis, and in the high turbulence regions close to the walls caused by the shearing effect of the flow at the no-slip boundaries.

## Notation

| | |
|---|---|
| $C_D$ | Stokes coefficient, dimensionless |
| $d_p$ | particle diameter, m |
| $h$ | half height of rectangular channel, m |
| $L_x^+, L_y^+, L_z^+$ | channel length in $(x^+, y^+, z^+)$ direction, dimensionless |
| $n_t$ | total number of particles in computational domain at time $t$, dimensionless |
| $Re_b$ | Reynolds number based on flow bulk velocity, dimensionless |
| $Re_p$ | particle Reynolds number, dimensionless |
| $Re_\tau$ | Reynolds number based on flow friction velocity, dimensionless |
| St | particle Stokes number, dimensionless |
| $t^+$ | time in wall units, dimensionless |
| $\Delta t^+$ | integration time-step in wall units, dimensionless |
| $u_x, u_y, u_z$ | fluid velocity components in $(x, y, z)$ directions, m s$^{-1}$ |
| $u_x{}^+, u_y{}^+, u_z{}^+$ | fluid velocity components in $(x^+, y^+, z^+)$ directions, dimensionless |
| $v_x{}^+, v_y{}^+, v_z{}^+$ | particle velocity components in $(x^+, y^+, z^+)$ directions, dimensionless |
| $u_\tau$ | shear velocity, m s$^{-1}$ |
| $U_x$ | time-averaged fluid velocity in streamwise direction, dimensionless |
| $U'^+_x, U'^+_y, U'^+_z$ | fluid velocity fluctuation components in $(x^+, y^+, z^+)$ directions, dimensionless |
| $U'^+_{x,rms}, U'^+_{y,rms}, U'^+_{z,rms}$ | time-averaged fluid velocity fluctuation components in $(x^+, y^+, z^+)$ directions, dimensionless |
| $U'^+_x U'^+_z$ | time-averaged-component of the Reynolds stress tensor, dimensionless |
| $u_b$ | bulk flow velocity in streamwise direction, m s$^{-1}$ |
| $x, y, z$ | Cartesian coordinate system, m |
| $x^+, y^+, z^+$ | Cartesian coordinate system in wall units, dimensionless |
| $\Delta x^+, \Delta y^+, \Delta z^+$ | grid resolution in $(x^+, y^+, z^+)$ directions, dimensionless |

*Greek letters*

| | |
|---|---|
| $\rho$ | fluid density, kg m$^{-3}$ |
| $\rho_p$ | particle density, kg m$^{-3}$ |
| $\tau_p$ | particle relaxation time, s |
| $\tau_w$ | wall shear stress, N m$^{-2}$ |
| $\nu$ | kinematic viscosity, m$^2$ s$^{-1}$ |

## References

Abdilghanie AM, Collins LR, Caughey DA. Comparison of turbulence modeling strategies for indoor flows. J Fluids Eng 2009;131:051402.
Armenio V, Fiorotto V. The importance of the forces acting on particles in turbulent flows. Phys Fluids (1994–present) 2001;13:2437–40.
Armenio V, Piomelli U, Fiorotto V. Effect of the subgrid scales on particle motion. Phys Fluids (1994–present) 1999;11:3030–42.
Alletto M, Breuer M. One-way, two-way and four-way coupled LES predictions of a particle–laden turbulent flow at high mass loading downstream of a confined bluff body. Int J Multiph Flow 2012;45:70–90.

Alvandifar N, Abkar M, Mansoori Z, Avval MS, Ahmadi G. Turbulence modulation for gas–particle flow in vertical tube and horizontal channel using four-way Eulerian–Lagrangian approach. Int J Heat Fluid Flow 2011;32:826–33.

Andersson HI, Zhao L, Barri M. Torque-coupling and particle–turbulence interactions. J Fluid Mech 2012;696:319–29.

Calvert G, Hassanpour A, Ghadiri M. Mechanistic analysis and computer simulation of the aerodynamic dispersion of loose aggregates. Chem Eng Res Des 2011;89:519–25.

Calvert G, Hassanpour A, Ghadiri M. Analysis of aerodynamic dispersion of cohesive clusters. Chem Eng Sci 2013;86:146–50.

Chen X, Li D, Luo K, Fan J. Direct numerical simulation of a three-dimensional particle laden plane mixing layer considering inter-particle collisions. Chem Eng Sci 2011;66:6232–43.

Chaumeil F, Crapper M. Using the DEM-CFD method to predict Brownian particle deposition in a constricted tube. Particuology 2014;15:94–106.

Chu K, Yu A. Numerical simulation of complex particle–fluid flows. Powder Technol 2008;179:104–14.

Crowe C, Troutt T, Chung J. Numerical models for two-phase turbulent flows. Annu Rev Fluid Mech 1996;28:11–43.

Crowe CT. On models for turbulence modulation in fluid–particle flows. Int J Multiphase Flow 2000;26:719–27.

Cundall PA, Strack ODL. A discrete numerical model for granular assemblies. Géotechnique 1979;29:47–65.

Deen N, Van Sint Annaland M, Van Der Hoef M, Kuipers J. Review of discrete particle modeling of fluidized beds. Chem Eng Sci 2007;62:28–44.

DEM-Solutions. EDEM coupling interface: programming guide; 2013.

Di Renzo DI, Cello A, Di Maio FFP. Simulation of the layer inversion phenomenon in binary liquid-fluidized beds by DEM-CFD with a drag law for polydisperse systems. Chem Eng Sci 2011;66:2945–58.

Elghobashi S. particle–laden turbulent flows: direct simulation and closure models. Appl Sci Res 1991;48:301–14.

Eskin D. Modeling dilute gas–particle flows in horizontal channels with different wall roughness. Chem Eng Sci 2005;60:655–63.

Fairweather M, Yao J. Mechanisms of particle dispersion in a turbulent, square duct flow. AIChE J 2009;55:1667–79.

Favier L, Daudon D, Donzé FV, Mazars J. Validation of a DEM granular flow model aimed at forecasting snow avalanche pressure. AIP Conf Proc 2009;1145:617–20.

Fraige F, Langston P. Horizontal pneumatic conveying: a 3d distinct element model. Granul Matter 2006;8:67–80.

Gao N, Niu J, He Q, Zhu T, Wu J. Using RANS turbulence models and Lagrangian approach to predict particle deposition in turbulent channel flows. Build Environ 2012;48:206–14.

Gatignol R. The Faxén formulae for a rigid particle in an unsteady non-uniform Stokes flow. J Theor Appl Mech 1983;1:143–60.

Germano M, Piomelli U, Moin P, Cabot WH. A dynamic subgrid-scale eddy viscosity model. Phys Fluids A: Fluid Dyn 1991;3:1760–5.

Humphrey CD, Cook E, Bradley DW. Identification of enterically transmitted hepatitis virus particles by solid phase immune electron microscopy. J Virol Methods 1990;29:177–88.

Jaszczur M. Large eddy simulations of particle–fluid interaction in a turbulent channel flow. J Phys: Conf Ser 2011;318:042052.

Johnson KL. Contact Mechanics. Cambridge: Cambridge University Press; 1985.

Johnson KL, Kendall K, Roberts AD. Surface energy and the contact of elastic solids. Proc R Soc Lond A Math Phys Sci 1971;324:301–13.

Kawaguchi H. Functional polymer microspheres. Prog Polym Sci 2000;25:1171–210.

Kim J, Moin P, Moser R. Turbulence statistics in fully developed channel flow at low Reynolds number. J Fluid Mech 1987;177:133–66.

Kim S-E. Large eddy simulation using an unstructured mesh based finite-volume solver. In: 34th AIAA fluid dynamics conference and exhibit; 2004. p. 1–7.

Kuang S, Chu K, Yu A, Zou Z, Feng Y. Computational investigation of horizontal slug flow in pneumatic conveying. Ind Eng Chem Res 2008;47:470–80.

Kuerten J. Subgrid modeling in particle–laden channel flow. Phys Fluids (1994–present) 2006;18:025108.

Kulick JD, Fessler JR, Eaton JK. Particle response and turbulence modification in fully developed channel flow. J Fluid Mech 1994;277:109–34.

Laín S, Sommerfeld M. Euler/Lagrange computations of pneumatic conveying in a horizontal channel with different wall roughness. Powder Technol 2008;184:76–88.

Laín S, Sommerfeld M. Effect of geometry on flow structure and pressure drop in pneumatic conveying of solids along horizontal ducts. J Sci Ind Res 2011;70:129–34.

Laín S, Sommerfeld M. Numerical calculation of pneumatic conveying in horizontal channels and pipes: detailed analysis of conveying behaviour. Int J Multiph Flow 2012;39:105–20.

Li J, Kuipers J. On the origin of heterogeneous structure in dense gas–solid flows. Chem Eng Sci 2005;60:1251–65.

Li J, Mason D. A computational investigation of transient heat transfer in pneumatic transport of granular particles. Powder Technol 2000;112:273–82.

Li J, Webb C, Pandiella S, Campbell G, Dyakowski T, Cowell A, Mcglinchey D. Solids deposition in low-velocity slug flow pneumatic conveying. Chem Eng Process: Process Intensif 2005;44:167–73.

Lilly D. A proposed modification of the Germano subgrid-scale closure method. Phys Fluids A: Fluid Dyn 1992;4:633–5.

Lim EWC, Wang CH, Yu AB. Discrete element simulation for pneumatic conveying of granular material. AIChE J 2006a;52:496–509.

Lim EWC, Zhang Y, Wang C-H. Effects of an electrostatic field in pneumatic conveying of granular materials through inclined and vertical pipes. Chem Eng Sci 2006b;61:7889–908.

Mangwandi C, Cheong YS, Adams MJ, Hounslow MJ, Salman AD. The coefficient of restitution of different representative types of granules. Chem Eng Sci 2007;62:437–50.

Marchioli C, Soldati A, Kuerten J, Arcen B, Taniere A, Goldensoph G, SQUIRES K, Cargnelutti M, Portela L. Statistics of particle dispersion in direct numerical simulations of wall-bounded turbulence: results of an international collaborative benchmark test. Int J Multiph Flow 2008;34:879–93.

Maxey MR, Riley JJ. Equation of motion for a small rigid sphere in a nonuniform flow. Phys Fluids 1983;26:883–9.

Mohaupt M, Minier J-P, Tanière A. A new approach for the detection of particle interactions for large-inertia and colloidal particles in a turbulent flow. Int J Multiph Flow 2011;37:746–55.

Nasr H, Ahmadi G. The effect of two-way coupling and inter-particle collisions on turbulence modulation in a vertical channel flow. Int J Heat Fluid Flow 2007;28:1507–17.

Ning Z. (Doctor of Philosophy thesis) Elasto-plastic impact of fine particles and fragmentation of small agglomerates (Doctor of Philosophy thesis). University of Aston; 1995.

Ning Z, Ghadiri M. Distinct element analysis of attrition of granular solids under shear deformation. Chem Eng Sci 2006;61:5991–6001.

Njobuenwu D, Fairweather M. Effect of shape on inertial particle dynamics in a channel flow. Flow Turbul Combust 2014;92:83–101.

Ouyang J, Yu A, Pan R. Simulation of gas–solid flow in vertical pipe by hard-sphere model. Part Sci Technol 2005;23:47–61.

Pan X, Liu X, Li G, Li T. Numerical investigation on gas–particle flows in horizontal channel under the reduced gravity environments. Acta Astronaut 2011;68:133–40.

Pan Y, Banerjee S. Numerical simulation of particle interactions with wall turbulence. Phys Fluids 1996;8:2733–55.

Pirker S, Kahrimanovic D, Kloss C, Popoff B, Braun M. Simulating coarse particle conveying by a set of Eulerian Lagrangian and hybrid particle models. Powder Technol 2010;204:203–13.

Pozorski J, Apte SV. Filtered particle tracking in isotropic turbulence and stochastic modeling of subgrid-scale dispersion. Int J Multiph Flow 2009;35:118–28.

Rhie C, Chow W. Numerical study of the turbulent flow past an isolated airfoil with trailing edge separation. AIAA J 1983;21:1525–32.

Robinson SK. Coherent motions in the turbulent boundary layer. Annu Rev Fluid Mech 1991;23:601–39.

Rowe PN, Enwood GA. Drag forces in hydraulic model of a fluidized bed – Part I. Trans Inst Chem Eng 1962;39:43–7.

Smagorinsky J. General circulation experiments with the primitive equations: I. The basic experiment. Mon Weather Rev 1963;91:99–164.

Squires KD, Eaton JK. Particle response and turbulence modification in isotropic turbulence. Phys Fluids A: Fluid Dyn 1990;2:1191–203.

Sundaram S, Collins LR. A numerical study of the modulation of isotropic turbulence by suspended particles. J Fluid Mech 1999;379:105–43.

Thornton C, Ning Z. A theoretical model for the stick/bounce behaviour of adhesive, elastic-plastic spheres. Powder Technol 1998;99:154–62.

Thornton C, Yin K. Impact of elastic spheres with and without adhesion. Powder Technol 1991;65:153–66.

Tsuji Y. Activities in discrete particle simulation in Japan. Powder Technol 2000;113:278–86.

Tsuji Y, Tanaka T, Ishida T. Lagrangian numerical simulation of plug flow of cohesionless particles in a horizontal pipe. Powder Technol 1992;71:239–50.

Vinkovic I, Doppler D, Lelouvetel J, Buffat M. Direct numerical simulation of particle interaction with ejections in turbulent channel flows. Int J Multiph Flow 2011;37:187–97.

Von Karman T. Calculation of pressure distribution on airship hulls. Technical Memorandums, National Advisory Committee for Aeronautics No. 574; 1930.

Vreman B, Geurts BJ, Deen N, Kuipers J, Kuerten J. Two-and four-way coupled Euler–Lagrangian large-eddy simulation of turbulent particle–laden channel flow. Flow Turbul Combust 2009;82:47–71.

Wang M, Lin C-H, Chen Q. Determination of particle deposition in enclosed spaces by Detached Eddy Simulation with the Lagrangian method. Atmos Environ 2011;45:5376–84.

Winkler C, Rani SL, Vanka S. A numerical study of particle wall-deposition in a turbulent square duct flow. Powder Technol 2006;170:12–25.

Xiang J, McGlinchey D. Numerical simulation of particle motion in dense phase pneumatic conveying. Granul Matter 2004;6:167–72.

Xu JQ, Zou RP, Yu AB. Analysis of the packing structure of wet spheres by Voronoi–Delaunay tessellation. Granul Matter 2007;9:455–63.

Yamamoto Y, Potthoff M, Tanaka T, Kajishima T, Tsuji Y. Large-eddy simulation of turbulent gas–particle flow in a vertical channel: effect of considering inter-particle collisions. J Fluid Mech 2001;442:303–34.

Zhang L, Thornton C. A numerical examination of the direct shear test. Geotechnique 2007;57:343–54.
Zhang M, Chu K, Wei F, Yu A. A CFD–DEM study of the cluster behavior in riser and downer reactors. Powder Technol 2008;184:151–65.
Zhao L. (Doctoral thesis) Particles in wall turbulence (Doctoral thesis). Norwegian University of Science and Technology; 2011.
Zhao L, Andersson HI, Gillissen J. Turbulence modulation and drag reduction by spherical particles. Phys Fluids 2010;22:081702.
Zhao L, Marchioli C, Andersson H. Stokes number effects on particle slip velocity in wall-bounded turbulence and implications for dispersion models. Phys Fluids 2012;24:021705.
Zhu H, Yu A. The effects of wall and rolling resistance on the couple stress of granular materials in vertical flow. Phys A: Stat Mech Appl 2003;325:347–60.
Zhu H, Zhou Z, Yang R, Yu A. Discrete particle simulation of particulate systems: a review of major applications and findings. Chem Eng Sci 2008;63:5728–70.